4-4-2023

Deposition, Material Characterization, and Mechanical Testing of Cr Containing Diamond-like Carbon Films

Nicholas Anderson
Louisiana State University and Agricultural and Mechanical College

DEPOSITION, MATERIAL CHARACTERIZATION, AND MECHANICAL TESTING OF Cr CONTAINING DIAMOND-LIKE CARBON FILMS

A Thesis

Submitted to the Graduate Faculty of the
Louisiana State University and
Agricultural and Mechanical College
in partial fulfillment of the
requirements for the degree of
Master of Science in Mechanical Engineering

in

The Department of Mechanical and Industrial Engineering

by
Nicholas Anderson
B.S., Louisiana State University, 2022
May 2023

Acknowledgments

This thesis was completed under the instruction of Dr. Wen Jin Meng. The amount of time Dr. Meng spent explaining theory, demonstrating the operation laboratory equipment, and processing experimental results is greatly appreciated. I thank Dr. Dorel Moldovan and Dr. Sunggook Park for serving on my advisory committee.

The other members of Dr. Meng's research group are greatly appreciated. Dr. Bin Zhang assisted in sample preparation, performing nano-indentation experiments, and performing cantilever bending tests. Dr. Xiaoman Zhang assisted in sample preparation, vacuum deposition processes, and X-ray diffraction measurements. Dr. Andrew Meng collected transmission electron microscopy data for the analyzed film system. Tailei Qi provided the background knowledge on the deposition of Diamond-like Carbon films.

Dr. Dongmei Cao and Dr. Yang Mu of Louisiana State University's Shared Instrument Facility provided valuable assistance in operating analytical instruments. Dr. Mu assisted in collecting X-ray photoelectron spectroscopy measurements.

Mr. Nicholas Dinecola and Mr. Roger Green of Louisiana State University's Advanced Manufacturing and Machining Facility produced sample substrates for friction and wear data collection. Dr. K. P. Lijesh of Dr. Michael Khonsari's research group collected friction and wear data.

This work was funded in part by the NSF EPSCoR program, under awards OIA-1541079 and OIA- 1946231. Partial project support through an NSF IUCRC, award IIP-2052810, is acknowledged. Use of experimental facilities at the MU Electron Microscopy Core (EMC) Facilities is acknowledged.

Table of Contents

Illustrations

Table

Figures

Abstract

A series of amorphous hydrogenated chromium containing diamond-like carbon films were deposited on 316 stainless steel substrates with a chromium interlayer through inductively coupled plasma assisted direct current magnetron sputtering. Details on the deposition process of these films are discussed. The film is characterized using scanning electron microscopy, X-ray photoelectron spectroscopy, X-ray diffraction, energy dispersive spectroscopy, and transmission electron microscopy. The coating hardness and indentation modulus is measured by instrumented nanoindentation. The coefficient of friction and the upper bound of the coating wear coefficient is measured using the pin-on-disk method. The fracture toughness of the diamond-like carbon film and a chromium film were measured to be 0.80 MPa $m^{1/2}$ and 2.50 MPa $m^{1/2}$ respectively. The fracture toughness of the interface between the coating and the substrate were measured by bending pre-notched microcantilever beams. The fracture surface of the cantilever beams was analyzed to measure the location of the crack propagation. The fracture toughness of the interface was found to vary approximately linearly between that of the diamond-like carbon film and that of chromium. The correlation was observed to depend on the area fraction of the fracture surface that occurred in the chromium interlayer.

Chapter 1. Introduction

1.1. Background and application of diamond-like carbon films

Diamond-like carbon (DLC) coatings belong to one class of amorphous carbon films. The films are called diamond-like due to their arrangement of sp^2 and sp^3 bonds, which correspond to the graphite and diamond phases of carbon respectively [1]. For classification purposes, amorphous carbon films are designated as a-C. Hydrogenated amorphous carbon films are designated as a-C:H. Amorphous carbon films with a higher content of sp^3 bonds compared to sp^2 bonds are designated as ta-C, where the "t" indicates a tetrahedral structure [2,3]. It has been widely documented that DLC coatings experience significant compressive stresses which scale with the film thickness [3]. To reduce the intrinsic residual stress within DLC coatings, many metal elements have been incorporated into the films [4-8]. Examples of metals incorporated into DLC films include Ti, Al, Co, Fe, Ni, W, and Cr [1]. It has also been documented that the incorporation of metals into DLC films leads to an increased in their fracture toughness [3]. Hydrogenated amorphous carbon films that have been alloyed with metals are indicated as a-C:H:Me, where "Me" is the metal incorporated into the film [3].

Diamond-like carbon films have been actively investigated since the 1980s due to their favorable mechanical properties. Some of the observed properties of DLC coatings are high hardness, chemical stability and inertness, low coefficient of friction, low wear rate, high infrared permeability, and optical transparency [1-3,9]. As a chemically inert material, DLC coatings have been used in a series of biomedical implants, including dental and cardiovascular implants [9,10]. Due to their observed low wear rate, DLC coatings have been used for medical implants around joints, specifically the hip and the knee [11-13]. Because the coatings have a low wear rate, it is less likely that the underlying material enters the bloodstream or muscle cells.

The low wear rate and low friction coeffects of DLC coatings make them useful in the extension of cutting tool life [14-16]. Diamond-like carbon has been explored as a material for Micro-electro-mechanical systems (MEMS) due to its higher Young's modulus and fracture toughness as compared to Si [17]. The combination of these properties allows for the development of high frequency resonant devices. The high wear resistance, high fracture toughness, and resistivity of DLC films has also been documented as beneficial for MEMS applications [18,19]. The DLC coating serves to protect the underlying structure.

1.2. Thin film deposition methods

Diamond-like carbon films were first deposited by Schmellenmeier in the 1950s [4]. The first use of the term "diamond-like carbon" was in the 1970s, when DLC films were deposited by ion beam deposition [4]. The deposition process used to deposit these films is described in [20]. In their ion bombardment system, there are two chambers of different pressures. A high-pressure discharge is used to introduce carbon ions from graphite electrodes to an Ar plasma source. Subsequent ion bombardment further sputters carbon ions where they can further be ionized in the plasma. The ionized carbon ions were then drawn into the deposition chamber using an auxiliary discharge. The two chambers were separated by a plasma constrictor. The substrate was given a negative bias voltage in order to attract the positively charged ions. Modern deposition techniques for depositing DLC films include evaporation, ion plating, pulsed laser deposition, laser arc deposition, and assorted sputtering techniques [4, 21].

Diamond-like carbon films have been deposited using electron-beam evaporation. In this process, a high-power electron beam is accelerated toward a carbon target, which causes the target to heat to the point of vaporization. The substrate is placed so the evaporated carbon ions will rise and infuse with the coating surface. The substrate can be heated in order to encourage

diffusion, but it was found that increased substrate temperature can cause a reduction in coating hardness [22]. The deposition rate of electron-beam evaporated DLC films has been recorded to be over 1 μm/min [22].

Arc ion plating has been used to deposit multilayer DLC films. In this deposition method, the source material is evaporated and ionized by electrical arcing. An advantage of arc ion plating is the relatively low pressure required for deposition. However, the substrate bias voltage applied during deposition can be significantly higher than that used in other deposition methods. Multilayer DLC coatings have been deposited at a base pressure of 2×10^{-2} Pa with a substrate bias voltage of -800 V [23].

In laser arc deposition, a pulsed laser beam strikes the surface of the carbon target to cause ablation. A magnetic field is also applied to direct the removed carbon ions toward the coating substrate. The deposition rate of DLC films deposited by laser arc deposition have been recorded on the order of 10 nm/min [24]. These films were recorded as having a coefficient of friction of approximately 0.1 and a surface roughness of 1.252 nm [24]. The surface roughness of deposited films has been observed to increase with film thickness.

The diamond-like carbon films deposited in this study were deposited by inductively coupled plasma (ICP) assisted direct current reactive magnetron sputtering. In this deposition method, the substrate and the target material are placed in a vacuum chamber. A plasma of an inert gas, typically Ar, is introduced. A negative voltage is applied to the target material to draw Ar^+ ions [25]. The target material is held by two magnets with opposite polarities, which focusses the Ar^+ plasma within a defined magnetic field. The surface of the target is bombarded by Ar^+ ions, resulting in the source material being sputtered towards the substrate. The assistance of a radio frequency ICP causes an increase in plasma density. The addition of a reactive gas,

specifically a hydrocarbon precursor such as butane or acetylene, allows for the deposition of hydrogenated carbon films [3]. One disadvantage of magnetron sputtering is that the applied magnetic field on the target material causes only a portion of the source to be sputtered [25].

Due to the limited yields of traditional magnetron sputtering, the deposition of DLC films by pulsed-direct current magnetron sputtering (pDCMS) and high-power impulse magnetron sputtering (HiPIMS) has been investigated. In both methods high-energy pulses are applied to the carbon source, causing more densely ionized source material to be directed toward the substrate. The deposition rate of DLC by pDCMS and HiPIMS have been recorded as 8.6 nm/min and 1.6 nm/min respectively [26]. The hardness of DLC films prepared by these methods was recorded as high as 30 GPa [26].

1.3. Objective of research

Over the past several decades, there has been a directive to collect quantitative data on the material properties of thin films. Before the emergence of focused ion beam (FIB) milling and micron scale mechanical testing coupled with scanning electron microscopy, many of the classification of film properties were either large scale or qualitative measurements. The tensile pull-off test involves adhering a 4” disk to the surface of a coating and pulling the disk and the substate apart [27]. The measured force of interfacial failure is measured and converted to a stress. Not only does this test require a relatively large surface area of coating, but also the applicability of the test is limited by the strength of the adherent between the coating and the disk. If the failure strength of the interface is greater than that of the cohesive strength of the adherent, this test cannot be used for the studied coating system [28]. A commonly utilized measure of film adhesion is the scratch test. In this test, an indenter with a known load is pressed into the film. The indenter is then moved while the load increases until the film begins to

delaminate from the substrate. The critical load at which delamination begins is recorded [29]. While the critical load can be used to rank different coating systems, it is difficult or impossible to correlate it to a standard material property.

Due to the development of FIB milling and the coupling of small-scale actuators with scanning electron microscopes, it has become possible to quantitatively measure the mechanical properties of thin films. In particular, the determination of fracture toughness by the fracture of micron-scale notched cantilever beams has been explored [30-34]. Through focused ion beam milling, it is possible to produce multiple micro-cantilever beams from the same film sample with a controllable notch depth. Details about this testing method are explored later in this document. The quantitative measurement of the fracture toughness of diamond-like carbon films is of interest, as the adhesion of DLC films to their substrates is an active area of research. The addition of a metallic adhesion layer or buffer layer between DLC films and their substrates have been found to improve film adhesion [35-37].

It is the objective of this study to quantify the fracture toughness of the interface of a a-C:H:Cr film with a Cr interlayer on stainless steel 316 (316SS) substrate. This study analyzes the effect of varying the Cr interlayer thickness on the measured fracture toughness of the coating-substrate interface. Cr interlayer thicknesses of 100, 200, and 300 nm are analyzed. In preparation of measuring this material property, this study also details the deposition parameters and material characterization of the described coating system.

Chapter 2. Deposition of Cr Containing Diamond-like Carbon

2.1. Vacuum deposition system

The diamond-like carbon films were deposited by radio frequency inductively coupled plasma assisted reactive magnetron sputtering. A schematic of the deposition system is shown in Figure 2.1. The system consists of two spherical chambers with six 6-inch diameter flanges. The uppermost flange connects a stepping motor to the sample holder. Two of the parallel flanges of the upper chamber connect sputtering guns and the sputtering targets to the system. The remaining two flanges utilize O-rings to allow the positioning of glass windows. The glass windows function as ports to insert sample substrates and to allow the transmission of time varying magnetic field from the externally placed radio frequency inductors into the deposition chamber. The glass windows are protected by ¼" thick aluminum oxide ceramic plates inside the system. Each ICP inductor consists of a planar copper spiral connected to a 13.56 MHz alternating current electric power supply. The sample holder is placed in the center of the upper

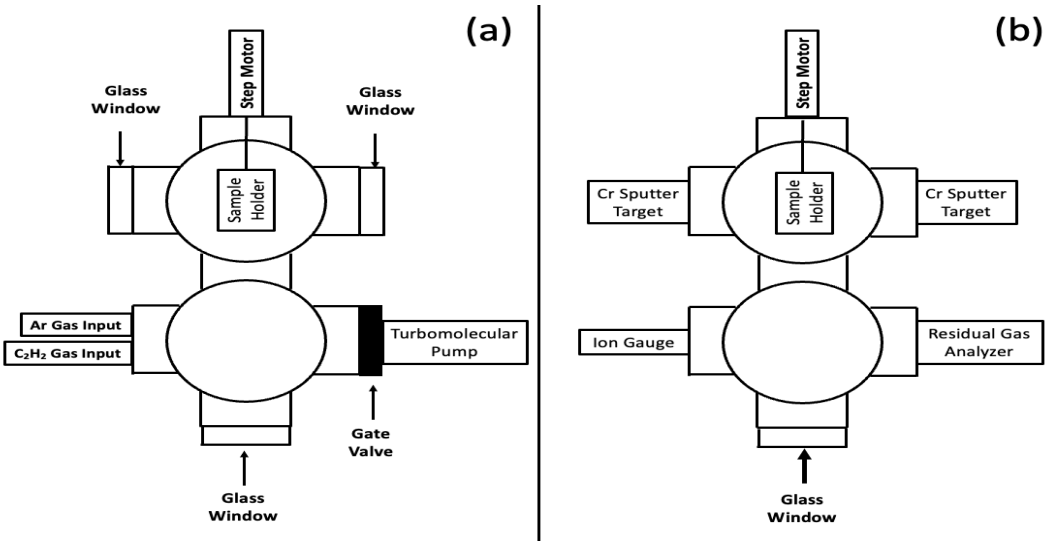

Figure 2.1. Schematic of the vacuum deposition system. Figure (a) is a front view of the system which allows the viewing of the turbomolecular pump, gas input lines, and the glass windows. Figure (b) is a side view that allows the viewing of the ion gauge, the residual gas analyzer, and the sputtering guns.

chamber in order to receive similar flux from the sputtering targets and experience a uniform plasma density.

The lowest flange on the system connects to a flange with an inlaid glass window so the operator can view the inside of the chamber during the deposition process. One flange connects the lower chamber to a turbomolecular pump through a gate valve. The turbomolecular pump is connected by a rotary vane pump which vents to an exhaust port. The operator can close the gate valve to manipulate the working pressure of the system. Another flange connects an ion gauge to the system to measure the system base pressure before deposition. A third flange connects a residual gas analyzer, which allows the operator to measure the pressure contributions of gas species by their molecular weight. The remaining flange connects the gas input lines to the deposition chamber. The gas input lines are connected to a flow meter with a controller to allow the operator to specify the input flow rate. In order to more quickly bring the system to a suitable vacuum, the system is wrapped with heating tape. To avoid compromising the seal of the glass windows with the O-rings and to avoid failure of the sputtering targets, the heating tape temperature is set so that the chamber walls do not exceed 80 °C.

2.2. Development of the deposition procedure

Flat 316SS sheets, ~1mm in thickness, were used as substrates for vapor deposition. Prior to deposition, the 316SS sheets were sequentially polished with 400, 600, 800, 1000, and 1200 grit sandpaper, followed by additional sequential polishing with 6 μm, 3 μm, and 1 μm diamond powders. After polishing, the substrates were cleaned with acetone and methanol, dried, and loaded into the deposition system. An elemental Cr layer was deposited between the a-C:H:Cr coating and the 316SS substrate as Cr is known empirically to be an effective adhesion promotor [38].

Sputter depositions occurred in a vacuum chamber with a base pressure below 1 x 10^{-7} Torr. Seventy-five mm diameter balanced magnetron sources were used with elemental Cr (99.9%+) targets. A 50 sccm Argon gas (99.999%+) input flow brought the working pressure to ~5.0 mTorr. An Ar inductively coupled plasma (ICP) was ignited within the deposition chamber using two planar spiral Cu induction coils outside the deposition chamber, coupled to the atmosphere inside the deposition chamber through two facing glass windows. The two Cu induction coils were powered by two separate 13.56 MHz radio frequency power supplies, with the total input power on each supply set to 500 W. The presence of this ICP elevates the plasma density inside the deposition chamber by at least one order of magnitude as compared to that for balanced magnetron sputtering without plasma assist [39]. The 316SS substrates were first etched in the Ar ICP for ~5 min, with a -50 V bias applied. Immediately after substrate etching, the Cr interlayer was deposited in the dc mode with a cathode current of 0.80 A, at a substrate bias of -50 V under the same total ICP input power of 1000 W. The a-C:H:Cr layer deposition commenced following Cr interlayer deposition. During a-C:H:Cr deposition, the Cr cathode current was reduced to 0.40 A, the substrate bias was increased to -150 V, and a 5.0 sccm C_2H_2 input flow was introduced into the system. The ICP input power was varied between 1000 W and 1200 W to keep the substrate bias current approximately a constant. The determination of the optimal substrate bias current is discussed further in the following paragraph. The substrate holder was connected to a 10 RPM stepping motor. The durations of Cr and a-C:H:Cr depositions were varied, respectively, to control the thicknesses of the Cr interlayer and the a-C:H:Cr layer. The deposition rate of the a-C:H:Cr layer was ~700 nm/hour. a-C:H:Cr/Cr/316SS specimens were fabricated with Cr interlayer thicknesses of 100, 200, and 300 nm and a a-

C:H:Cr layer of 2.5 – 3.0 μm in thickness. An elemental Cr film of ~2.5 μm in thickness was deposited separately using the same deposition parameters as those used for the Cr interlayers.

Many of the deposition procedures described above were used in depositions by a previous graduate student. However, simply reproducing the external equipment parameters did not repeatably produce dense, uniform, and adherent coatings. It was found that while all operator inputted deposition parameters could be identical, the internal conditions of the deposition plasma could vary. The two primary causes of this variability were the system base pressure and the condition of the protective aluminum oxide ceramic plates. First, if the system base pressure was not at a suitable level, residual water vapor would affect the purity of the Ar+ plasma and therefore reduce the substrate bias current. Second, if the ceramic plates had too thick of a coating from previous depositions, the amount of ICP input power that entered the system would be lower. This would also cause the substrate bias current to decrease. The described electrical shielding effect appeared to be more pronounced when metal films were deposited.

Through a series of depositions, it was determined that the optimal substrate bias current for depositing the a-C:H:Cr layer was between 0.75 A – 0.78 A. The total ICP input power was varied between 1000 W – 1200 W to ensure that the substrate bias current was in this range. Figure 2.2 shows films deposited with different substrate bias currents. The film in Figure 2.2(a) was deposited with a substrate bias current of 0.61 A. There is a high density of particulates on the surface of the film and there are apparent voids inside the film. The film in Figure 2.2(b) was deposited with a substrate bias current within the above listed range. A film deposited with a substrate bias current of 0.80 A immediately delaminated from the substrate.

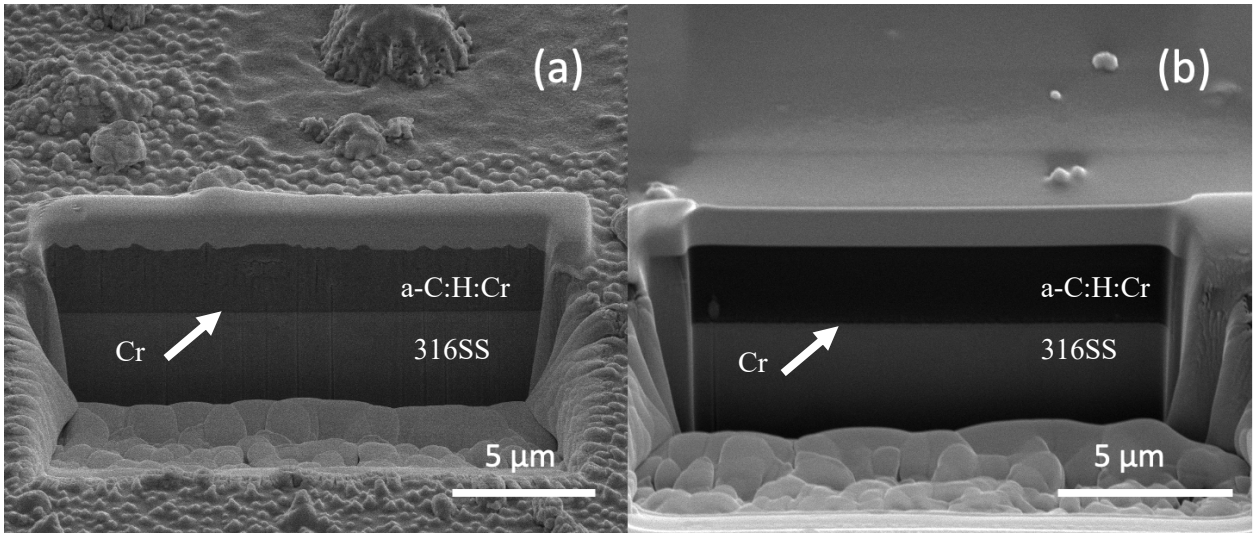

Figure 2.2. Cross section images of films grown with different substrate bias currents. Figure (a) is a film grown with a substrate bias current of 0.61 A. Figure (b) is a film grown with a substrate bias current of 0.75 A.

2.3. Discussion

Using the vacuum deposition system and deposition parameters described above, the author of this study was able to repeatably produce uniform, void free coatings with a relatively low level of surface or imbedded particulates. Understanding the effect of the substrate bias current on the quality of the deposited film was the most challenging aspect of producing consistent films. The substrate bias current is a measure of the rate of ionized particulates impacting the surface of the film. As the substrate bias current increases, the amount of deposited film that is etched from the substrate increases. Therefore, it is reasonable to assume that a higher substrate bias current would produce dense films with few particulates on the surface. However, the higher etching rate also increases the residual stress in the film, which can lead to delamination. Once the suitable range for the substrate bias current was found, the operator of the deposition system had to manipulate the external deposition parameters, specifically the ICP input power, to produce the correct internal plasma parameter.

Chapter 3. Material Characterization of Coating System

3.1. Surface morphology

The quality of deposited films was analyzed using scanning electron microscopy (SEM) and focused ion beam milling (FIB). All film samples were analyzed using a Quanta^{TM} 3D DualBeam^{TM} FEG FIB-SEM. The cross section of the film was analyzed by using FIB milling to create a 20 μm x 10 μm rectangular hole with a depth of at least 5 μm. A 20 μm x 3 μm rectangular layer of platinum with a thickness of 2 μm was deposited to protect the surface of the film while milling. Images of the film were then taken using a secondary electron (SE) detector at a 52° angle. Examples of the cross-sectional images taken of the films is shown in Figure 2.2. Film quality was determined by visually inspecting the amount of particulates on the film surface, the presence of voids or imbedded particulates in the film layer, and the uniformity of the 316SS – Cr and Cr – a-C:H:Cr interfaces.

3.2. X-ray photoelectron spectroscopy

The presence of intended elements and impurities within deposited coating layers were determined using a Scienta Omicron ESCA 2SR X-ray Photoelectron Spectroscope (XPS). In X-ray photoelectron spectroscopy, X-rays with an energy of hν, where h is Planck's constant and ν is the frequency of the X-rays, are directed towards the surface of the sample. The interaction between the X-rays and the sample can cause electrons to release from the sample surface. The energy balance described in Equation 3.2 provides the relationship between the energy of the incident X-rays, the binding energy BE of the ejected electrons, the kinetic energy KE of the ejected electrons, and the spectroscope work function Φ [40].

$$KE = h\nu - BE - \Phi \quad \text{(Equation 3.2)}$$

In the spectroscope used, a monochromatic Al Kα excitation source was used. XPS spectra were acquired from coating layer surfaces, either in the as-deposited state after removal from the deposition system or after ion sputter etching with a 5 kV 10 mA Ar^+ ion beam for 20-40 min. Etching can be required depending on the sample exposure to air and other contaminants. As the escape depth of electrons is only several nanometers, removing any contamination layer from the surface can be necessary to determine the true composition of the film [40]. Survey scans in the binding energy range of 0–1200 eV in 1 eV steps were acquired immediately after ion etching. Raw XPS data were processed using CasaXPS.

Figure 3.1 shows the results of the compositional characterization of a-C:H:Cr/Cr/316SS specimens by XPS. Figures 3.1(a) and 3.1(b) show respectively two XPS spectra collected from the top surface of one a-C:H:Cr layer, in the as-deposited state and after Ar^+ ion etching. O 1s signal is present in the as-deposited state, which decreases to background level after ion etching. N 1s and Ar 2p signals are close to background level in the as-deposited state, but increase after ion etching. Figure 3.1(c) shows one XPS spectrum collected from the top surface of another elemental Cr layer deposited onto a 316SS substrate, after Ar^+ ion etching. Only signals from Cr core levels and Auger transitions are present. Data shown in Fig. 3.1 indicate that O and N impurities within the present series of a-C:H:Cr/Cr/316SS specimens are below the XPS detection limit, ~1 at.% and that no significant impurities are detected near the top of the Cr interlayer.

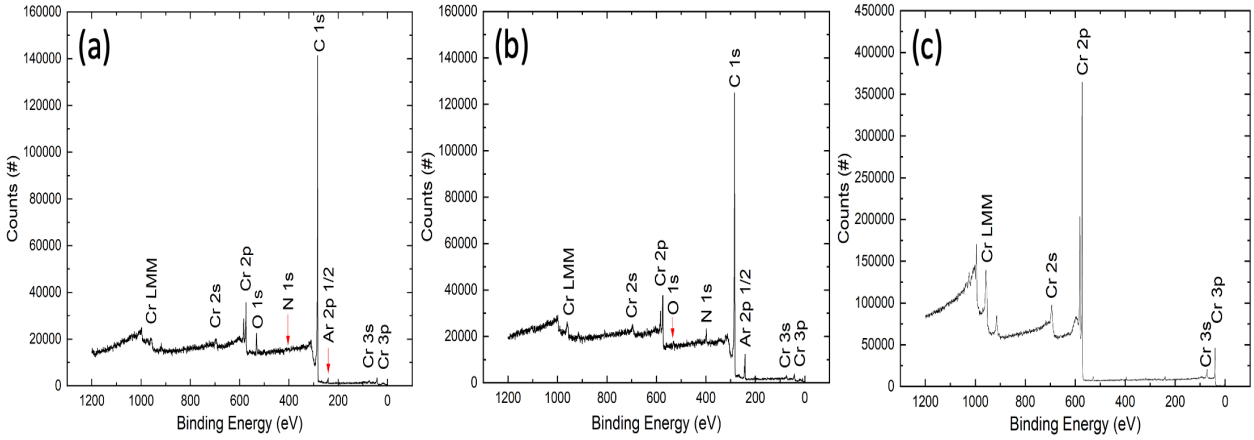

Figure 3.1. Compositional characterization of a-C:H:Cr/Cr/316SS specimens: (a) an XPS spectrum acquired from the top surface of one a-C:H:Cr layer in the as-deposited state; (b) an XPS spectrum of the same a-C:H:Cr layer after Ar^+ ion sputter etching. The red arrows in (a) and (b) highlight respectively spectral locations for O 1s, N 1s, and Ar 2p; (c) an XPS spectrum acquired from the top surface of one Cr layer deposited on 316SS after Ar^+ ion sputter etching.

High-resolution scans around the C 1s peak and Cr 2p peak were also taken. The same XPS acquisition parameters were used with the exception of the binding energy step size being reduced. The purpose of collecting high-resolution surveys around these two binding energies was to determine whether there was a binding energy shift of either peak due to change in the atomic bonding environment. Figure 3.2(a) displays the measured intensity peak near the C 1s binding energy. In addition to signal due to C-C bonding at a binding energy of ~285 eV, two additional peaks arise, which can be identified to be due to C-O bonding and C-Me bonding. The latter is consistent with the presence of C-Cr bonds [40]. Figure 3.2(b) displays the measured intensity peaks near the Cr $2p_{1/2}$ and the $2p_{3/2}$ binding energies of 583 and 574 respectively [40]. Upon processing, it was also found there is contribution to these signals from two bond types. The significance of these the presence of both C-C and C-Cr bonds will be discussed again in the discussion of the transmission electron microscopy (TEM) performed on the coating system.

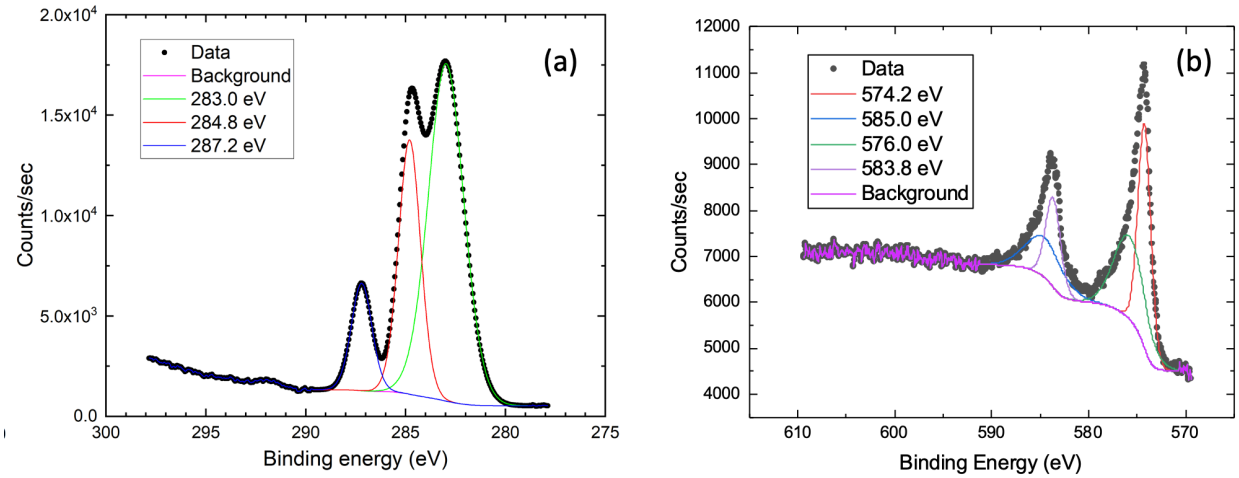

Figure 3.2. High-resolution binding energy spectrum for C 1s and Cr 2p bonds. (a) an XPS spectrum of an as-deposited a-C:H:Cr film around the C 1s bond binding energy. (b) an XPS spectrum on an etched a-C:H:Cr film around the Cr 2p bond binding energy.

3.3. X-ray diffraction

X-ray diffraction (XRD) characterization was carried out using a PANalytical Empyrean system with Cu Kα radiation. XRD data were analyzed with the PANalytical HighScore^{TM} software packages. In X-ray diffraction, incident X-rays with a known wavelength are directed towards the surface of a sample at a certain angle θ. Due to the wavelength of the X-rays λ and the interplanar spacing d_{hkl} of the crystal planes in the sample, the X-rays can either remain in phase or destructively interfere. The proper angle to keep X-rays in phase and constructively interfere is defined by Bragg's Law in Equation 3.3 [41] in which the term n indicates the order of diffraction.

$$n\lambda = 2d_{hkl}\sin(\theta) \quad \text{(Equation 3.3)}$$

Figure 3.3 shows a θ/2θ XRD pattern from the a-C:H:Cr/Cr/316SS specimen. Aside from the diffraction peaks indexed to the Austenite structure of the 316SS substrate, the only other crystalline diffraction peak present in the pattern is indexed to that of Cr (200). This diffraction peak can be attributed to a crystalline Cr interlayer combined with any signal coming from the a-

C:H:Cr layer. It is possible that a portion of this signal comes from a B1 chromium carbide structure within the a-C:H:Cr layer. This possibility is discussed further in the TEM analysis.

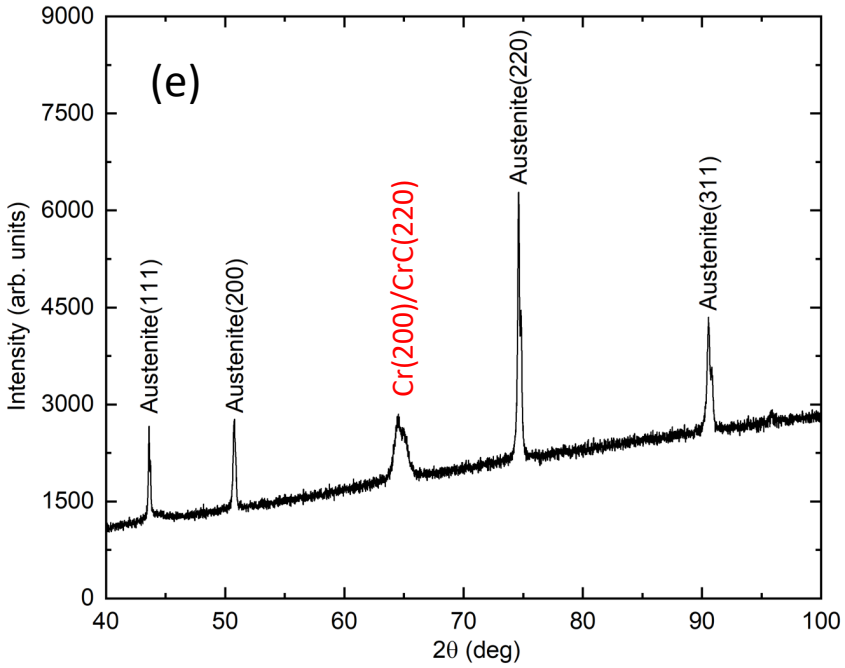

Figure 3.3. θ/2θ XRD pattern obtained from one a-C:H:Cr/Cr/316SS specimen with indexed diffraction peaks.

3.4. Transmission electron microscopy

Transmission electron microscopy (TEM) characterization was conducted on as-deposited a-C:H:Cr/Cr/316SS cross-sectional specimens using a spherical aberration probe-corrected ThermoFisher Spectra 300 Scanning/Transmission Electron Microscope (S/TEM). The microscope is equipped with a Super-X EDS silicon drift detector system with a 0.7 sr solid angle. Cross-sectional TEM imaging, selected area diffraction patterns (SADPs), and STEM-EDS mapping were conducted. TEM cross-section samples were lifted out using a FEI Quanta 3D DualBeam FEG Ga^+ focused ion beam/scanning electron microscope (FIB/SEM) with final thinning performed at 5 kV.

Cross-sectional specimens were prepared by FIB milling a lamella using a Helios™ G4 PFIB CXe DualBeam™ FIB/SEM. The lamella was polished using a low FIB current to reduce the thickness below 100 nm. The lamella included portions of the 316SS substrate, the Cr interlayer, and the a-C:H:Cr film to both analyze crystal structure and view the coating system interfaces.

Figure 3.4 shows results of structural characterization of a-C:H:Cr/Cr/316SS specimens by TEM/STEM. Figure 3.4(a) shows a cross-sectional TEM image of one a-C:H:Cr/Cr/316SS specimen, in which the 316SS substrate, the Cr interlayer, and the a-C:H:Cr top layer are shown clearly. The thickness of the Cr interlayer is ~200 nm. Selected area electron diffraction patterns are collected from the 316SS substrate, the Cr interlayer, and the a-C:H:Cr top layer regions and shown respectively in Figs. 3.4(b), 3.4(c), and 3.4(d), with placements of the selected area aperture indicated approximately by the red circles marked 1, 2, and 3 in Fig. 3.4(a). The SADP displayed in Fig. 3.4(b) shows crystalline diffraction spots from the 316SS substrate. The SADP displayed in Fig. 3.4(c) shows a clear, indexed polycrystalline ring pattern consistent with that from a BCC structure, indicating that the Cr interlayer is polycrystalline BCC, as expected. The SADP displayed in Fig. 3.4(d) shows polycrystalline diffraction rings superimposed on a diffuse background. While the diffuse background is consistent with the expected amorphous structure of a-C:H, the diffraction rings present in Fig. 3.4(d) are identical to those shown in Fig. 3.4(c), indicating that the crystalline phase present within the a-C:H:Cr layer is BCC Cr. Two possible explanations for this observation are possible. The first is that there are crystalline Cr particulates in the a-C:H:Cr layer. The second is that there are chromium carbide particulates that generate similar lattice spacings to that of BCC Cr. This corresponds with the observation made in the analysis of Figure 3.3.

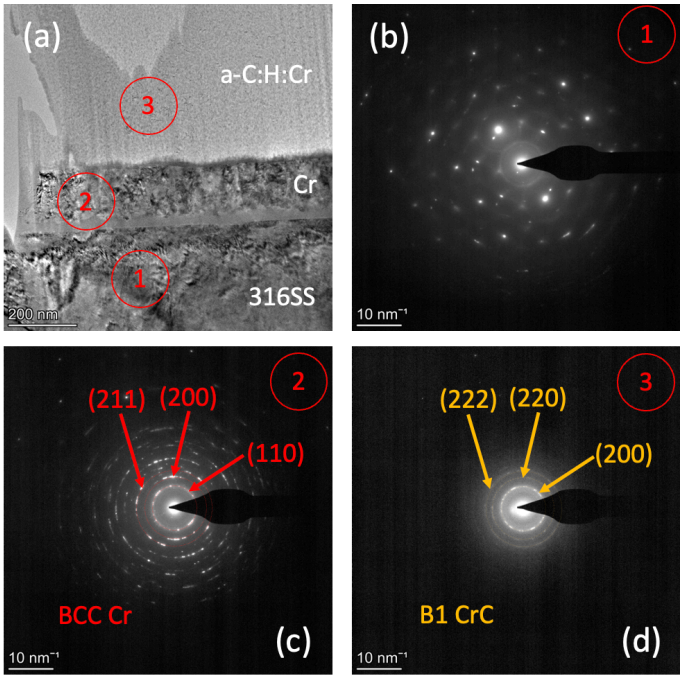

Figure 3.4. TEM characterization of Cr-DLC coated 316SS: (a) cross-section TEM image; (b/c/d) SADPs obtained respectively from the 316SS substrate, Cr interlayer, and a-C:H:Cr layer regions. The placement of the SAD apertures is indicated approximately by the red circles 1, 2, and 3 in (a).

Figure 3.4(a) also shows two thin transition layers at the Cr/316SS and a-C:H:Cr/Cr interfaces, which are devoid of diffraction contrast. Figure 3.5 shows the results of cross-section STEM characterization of the a-C:H:Cr/Cr interfacial region. Figures 3.5(a) and 3.5(b) show respectively cross-section STEM EDS intensity maps of C Kα and Cr Kα. As one traverses from the Cr interlayer (bottom of figure) into the a-C:H:Cr top layer (top of figure), the Cr intensity decreases and gives way to a uniform C intensity, as expected. Figure 3.5(c) shows the corresponding high angle annular dark field (HAADF) cross-section image of the a-C:H:Cr/Cr interfacial region. Figure 3.5(d) shows the result of quantification of a STEM EDS line scan from within the Cr interlayer region into the a-C:H:Cr top layer region with the line scan path approximately perpendicular to the interface, as indicated by the light blue arrow in Fig. 3.5(c). The EDS line scan indicates that a compositionally graded transition layer exists at the a-

C:H:Cr/Cr interface, with the thickness of the transition layer being ~40 nm. As the ICP was kept on during the entire deposition process, this compositionally graded transition layer can be consistent with ion-induced compositional mixing at the interface, which is accentuated by the much higher ion flux due to the high plasma density of the ICP. The average Cr composition within the a-C:H:Cr layer is ~40 at.% according to the EDS data shown in Fig. 3.5(d). A similar compositionally mixed region is observed at the Cr/316SS interface.

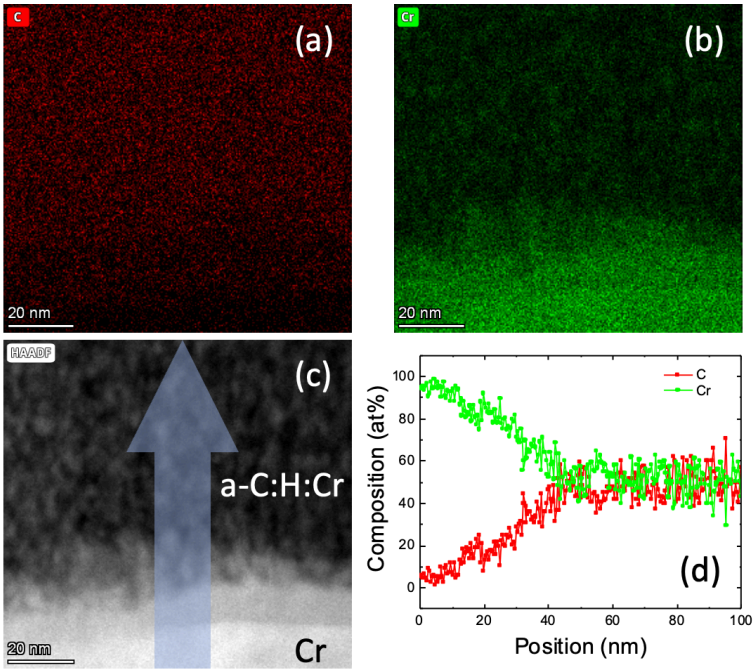

Figure 3.5. STEM characterization of interfacial region between the a-C:H:Cr top layer and the Cr interlayer: cross-section STEM EDS intensity map of (a) C; (b) Cr; (c) HAADF cross-section image of the a-C:H:Cr/Cr interfacial region; (d) quantification of STEM EDS line scan, with the line scan path indicated by the light blue arrow in (c).

Figure 3.6 shows the results of cross-section STEM characterization of the a-C:H:Cr top layer from a thinner region as compared to the a-C:H:Cr region shown in Fig. 3.5. Figures 3.6(a) and 3.6(b) show respectively cross-section STEM EDS intensity maps of C Kα and Cr Kα. While more uniform C Kα and Cr Kα intensities are shown in Fig. 3.5, Fig. 3.6(b) shows apparent nanoscale Cr clustering. The corresponding cross-section HAADF image is shown in

Fig. 3.6(c), in which nm scale cluster contrast is also present due to Z contrast, consistent with the EDS mapping information shown in Fig. 3.6(b). Figure 3.6(d) shows the result of the quantification of a STEM EDS line scan within the a-C:H:Cr top layer region, with the line scan path indicated by the light blue arrow in Fig. 3.6(c). BCC Cr nanoparticles in thicker regions can overlap with each other sufficiently in the electron beam direction to exhibit seemingly uniform average C and Cr composition; this cannot occur when the sample thickness decreases below a threshold. The variation in TEM sample thickness can be attributed to an inherent tapering of the focused ion beam. Data shown in Figs. 3.4 and 3.5 combined can indicate that the a-C:H:Cr layer consists with nm sized BCC Cr clusters embedded in an a-C:H matrix. However, it is still possible that the particulates are of a chromium carbide particulate that has a similar lattice parameter to that of BCC Cr. The combined XPS, XRD, and TEM data cannot be used to definitively state whether these particulates are purely chromium or a chromium carbide.

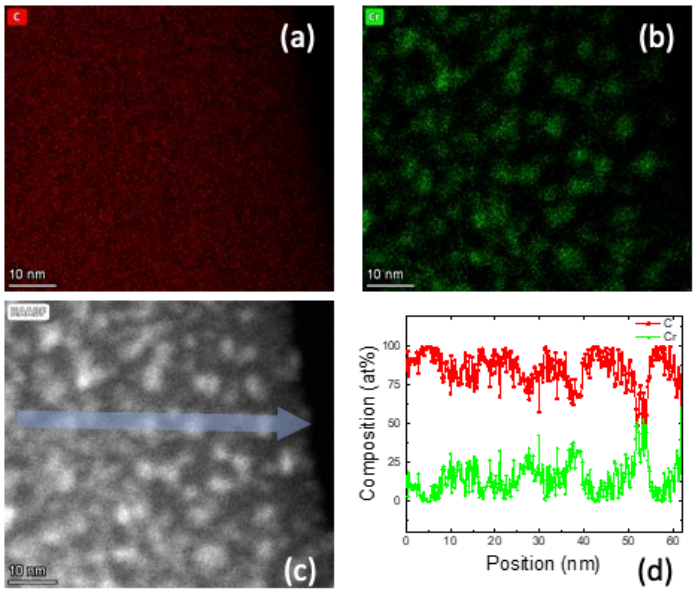

Figure 3.6. STEM characterization of the a-C:H:Cr layer: cross-section STEM EDS intensity map of (a) C; (b) Cr; (c) HAADF cross-section image of the a-C:H:Cr layer; (d) quantification of STEM EDS line scan, with the line scan path indicated by the light blue arrow in (c).

3.5. Discussion

A comprehensive characterization of the elemental composition and microstructure of the a-C:H:Cr/Cr/316SS coating system has been performed. The surface and interfacial morphology were viewed using SEM imaging. The deposited films were determined to have uniform interfaces. There were no obvious voids or imbedded particulates in the film layers that would result in improperly measured film mechanical properties. EDS measurements which were coupled with TEM imaging agrees with the measured XPS spectrums that the elements present in the a-C:H:Cr layer are primarily C and Cr. There is no significant oxygen or nitrogen impurity viewed in the measured XPS spectrum after etching the surface of the film.

Both XPS and TEM data indicate that there are nanometer scale particulates within the a-C:H matrix of the DLC portion of the film. High-resolution XPS measurements around the C 1s and Cr 2p binding energies indicated the presence of both C-C and C-Cr bonds. However, based on these surveys alone the ratio of these bonds could not be determined. Based on the TEM images coupled with the corresponding EDS mapping, it is not clear whether these particulates are BCC Cr or a chromium carbide. The same can be stated for the collected diffraction rings. Further investigation of the composition of these particulates is outside the scope of this study.

Chapter 4. Mechanical Testing of Coating System

4.1. Nanoindentation testing

Instrumented nanoindentation was carried out on an MST NanoIndenter XP instrument with a diamond Berkovich indenter. Hardness and indentation modulus were measured as a function of the indentation depth. Ten repeat measurements were conducted at each load/indentation depth. Details about the nanoindentation testing to determine hardness and indentation modulus can be found in [42]

Figure 4.1 shows the results of hardness and modulus measurements by instrumented nanoindentation. Figure 4.1(a) shows hardness values vs. indentation depth measured from one a-C:H:Cr/Cr/316SS specimen and one uncoated 316SS substrate. Hardness values (H) measured from the uncoated 316SS shows an increase with decreasing indentation depth (h). The inset in Fig. 4.1(a) shows H^2 plotted vs. 1/h, the linear proportionality between H^2 and 1/h shows the expected indentation size effect on uncoated 316SS. Measured H values for the a-C:H:Cr/Cr/316SS specimen also increases with decreasing h. At small h values, an approximate hardness plateau is reached with an H value of ~7.5 GPa. Figure 4.1(b) shows, as a function of the indentation depth, corresponding values of indentation modulus, $E/(1-\nu^2)$, where E and ν are respectively the Young's modulus and the Poisson's ratio. For the uncoated 316SS, measured values of the indentation modulus are close to 225 GPa, consistent with expected values of E = 205 GPa and $\nu = 0.3$ for 316SS. For the a-C:H:Cr/Cr/316SS specimen, the measured indentation modulus decreases with decreasing indentation depth, and reaches an approximate plateau with an $E/(1-\nu^2)$ value of ~75 GPa. The values of 7.5 GPa and 75 GPa are taken as being representative of the hardness and indentation modulus of the present a-C:H:Cr or Cr-DLC layer.

The fact that the value of H/E for the present Cr-DLC is ~0.1 is also consistent with previous results on Me-DLC coatings [43].

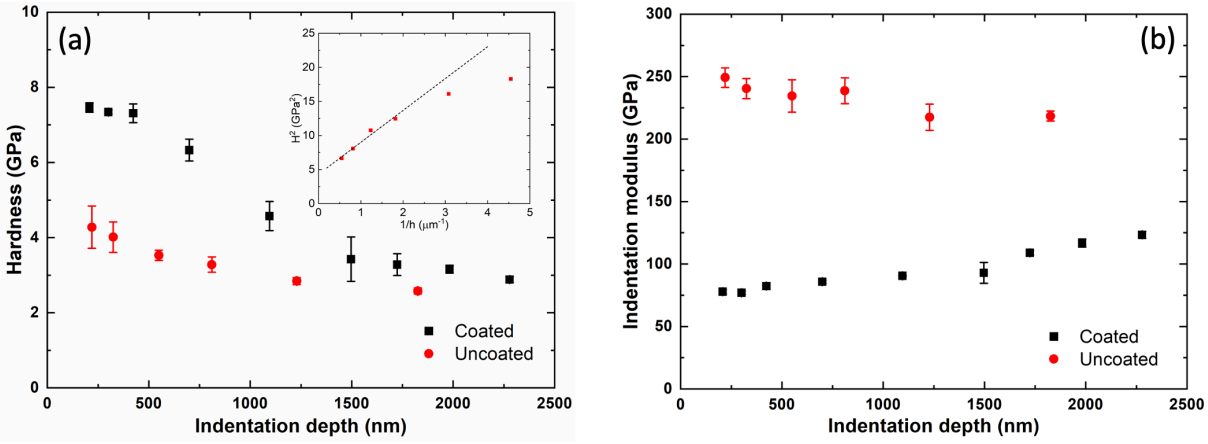

Figure 4.1. Instrumented nanoindentation of Cr-DLC coated and uncoated 316SS substrates: (a) hardness and (b) indentation modulus plotted vs. indentation depth. The inset in (a) is a plot of H^2 vs. 1/h for the uncoated 316SS specimen.

4.2. Friction and wear characteristics

Evaluation of sliding friction and wear characteristics was conducted with a pin-on-disk setup on a Bruker Universal Mechanical Tester (UMT) instrument. Dry sliding occurred between uncoated and Cr-DLC coated 316SS coupons and 304 stainless steel balls of diameters ranging from 3 to 12.6 mm, at linear velocities ranging from 0.15 to 0.50 m/s. At normal loads ranging from 1.5 to 10 N, the nominal Hertzian contact pressures ranged from 0.45 to 2.18 GPa.

Figure 4.2 shows the results of the pin-on-disk evaluation of sliding friction and wear characteristics. The purple trace displaced in Fig. 4.2(a) show the measured friction coefficient due to dry sliding contact between a 304 stainless steel ball and an uncoated 316SS coupon, at a Hertzian contact pressure of 0.45 GPa and a sliding speed of 0.15 m/s. As a function of time, the friction coefficient exhibits large variations, ranging between 0.6 and 0.8. The red and blue traces in Fig. 4.2(a) show measured friction coefficients due to dry sliding contact between a 304 stainless steel ball and a Cr-DLC coated 316SS coupon at Hertzian contact pressures of 1.06 and

1.33 GPa, respectively. The presence of the a-C:H:Cr/Cr layers between the 304 stainless steel ball and the 316SS substrate leads to a much lower friction coefficient of ~0.2, with much lower variations. Figure 4.2(b) shows an SEM image of the wear track on the uncoated 316SS coupon after a total sliding distance of ~525 m at a Hertzian contact pressure of 0.45 GPa. Without quantifying the wear volume, it is evident from Fig. 4.2(b) that severe wear has occurred within the wear track, generating a large amount of wear debris that piled up outside the wear track.

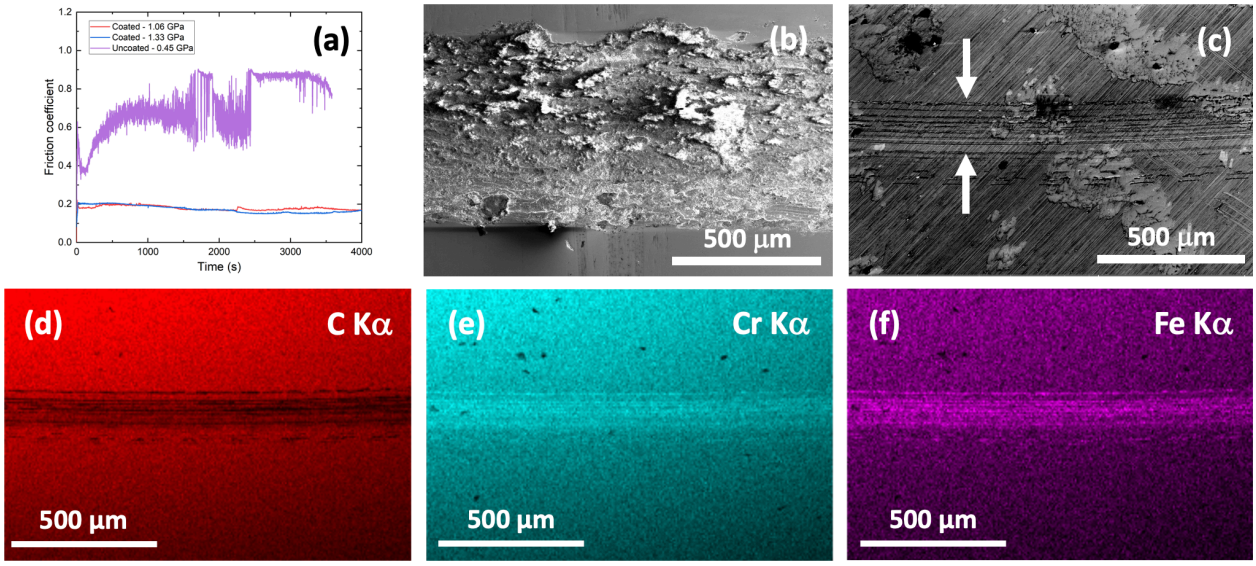

Figure 4.2. Dry friction and wear of Cr-DLC coated and uncoated 316SS: (a) sliding friction coefficient of uncoated and Cr-DLC coated 316SS coupons at different contact pressures; (b) an SEM image of the wear track on the uncoated 316SS at 0.45 GPa contact pressure; (c) an SEM image of the wear track on the Cr-DLC coated 316SS at 0.45 GPa contact pressure; (d/e/f) EDS intensity maps of C Kα, Cr Kα, and Fe Kα on the wear track shown in (c). White arrows in (c) highlight the location of the wear track.

Figure 4.2(c) shows an SEM image of the wear track on the Cr-DLC coated 316SS coupon after a total sliding distance of ~525 m at a normal load of 1.5 N and a Hertzian contact pressure of 0.45 GPa. Figures 4.2(d/e/f) shows the corresponding EDS intensity maps of C Kα, Cr Kα, and Fe Kα, respectively. As compared to areas outside the wear track, the Cr Kα and Fe Kα intensity have increased within the wear track, while the C Kα intensity has decreased but not eliminated. Data displayed in Figs. 4.2(c-f) show that, while wear has occurred, the a-C:H:Cr

layer has not been completely removed within the wear track. Taking into account the wear track width measured from Fig. 4.2(c) of ~180 μm, the thickness of the a-C:H:Cr layer of ~700 nm, and the normal load of 1.5 N, an upper bound on wear rate and wear coefficient can be estimated to be, respectively, 2.1×10^{-5} mm^3/m and ~1.4×10^{-5} $mm^3/(N\ m)$, by assuming the removal of the entire a-C:H:Cr layer within the observed wear track width. This order of magnitude estimate of dry sliding wear coefficient is in accordance with previously reported values for Me-DLCs [44]. Data shown in Fig. 4.2(a) further indicate that gradual wear of Cr-DLC occurred under dry sliding between 304 stainless steel ball and Cr-DLC coated 316SS coupon up to ~1.3 GPa of Hertzian contact pressure without inducing spallation at or failure of the Cr-DLC/substrate interfaces.

4.3. Determination of fracture toughness via notched microcantilever beams

Microcantilever beam specimens were fabricated with FIB milling on the Quanta 3D FIB/SEM. One set of microcantilever beams consisting entirely of the a-C:H:Cr coating layer was fabricated to determine the fracture toughness of the Cr-DLC. Another set of microcantilever beams was fabricated entirely out of a ~2.5 μm thick elemental Cr layer deposited onto a 316SS substrate following the same procedure used for depositing Cr interlayers between the a-C:H:Cr layer and the 316SS substrate. A third set of microcantilever beams was fabricated to reveal the a-C:H:Cr/Cr/316SS interfacial region, with FIB milled pre-notches located within the Cr interlayer. The dimensions of as-fabricated microcantilever beams were determined through high resolution SEM imaging on a ThermoFisher Helios™ G4 Xe+ plasma focused ion beam/scanning electron microscope system (PFIB/SEM). Using this equipment, images with a magnification of 100,000 were collected with reasonable focus.

Bending of the microcantilever beams was conducted in-situ the Quanta 3D FIB/SEM using a FemtoTools NMT-04 system, using either a ~1 μm diameter Si punch or a ~2 μm x 2 μm Si punch. The load force, punch displacement, and a SEM video of the microcantilever beams under bending load were recorded. Loading proceeded in displacement control, with displacement rates ranging from 20 nm/sec to 50 nm/sec.

Fracture toughness values of the a-C:H:Cr layer, the Cr layer, and the interfacial region between the a-C:H:Cr layer and the 316SS substrate were determined by bending of microcantilever beams with FIB milled pre-notches in accordance with the procedure outlined in [31]. Figure 4.3 shows typical microcantilever beams fabricated by FIB milling. Figure 4.3(a) shows one beam consisting entirely of the a-C:H:Cr layer, with the Cr interlayer and 316SS substrate underneath removed and a pre-notch cut into the beam top surface. Figure 4.3(b) shows one beam milled with the specimen placed in a 90° rotated orientation, exposing the a-C:H:Cr layer with a thickness of ~3 μm, the Cr interlayer with a thickness of ~300 nm, and the 316SS substrate. A pre-notch was FIB milled into the middle of the Cr interlayer top surface. A Pt layer was deposited onto the a-C:H:Cr top surface for protection during FIB milling. The protective Pt layer does not influence the bending data as the bending load was applied on a-C:H:Cr. A separate elemental Cr layer, ~3 μm in thickness, was deposited onto a 316SS substrate following the same deposition procedure for Cr interlayers.

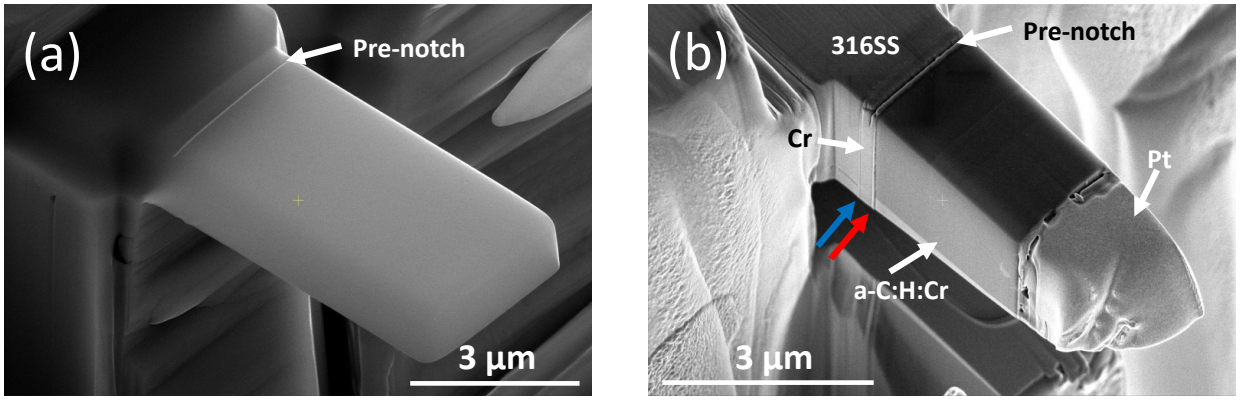

Figure 4.3. Microcantilever beams fabricated by FIB milling: (a) one beam milled entirely within the a-C:H:Cr coating layer; (b) one beam exposing the a-C:H:Cr layer, the Cr interlayer, and the 316SS substrate. A FIB milled pre-notch was cut into the top DLC coating surface in (a) and the middle of the Cr interlayer top surface in (b). The blue and red arrows in (b) highlight the locations of the 316SS/Cr and Cr/a-C:H:Cr interfaces.

Separate microcantilevers consisting entirely of the Cr layer were fabricated, analogous to the a-C:H:Cr cantilever shown in Fig. 4.3(a). Pre-notched Cr microcantilever bending was conducted to measure the fracture toughness of the deposited Cr layer. The microcantilever beam width B and thickness in the loading direction W were measured before the test by averaging a minimum of three measurements taken from SEM images. The depth of the pre-notch a was measured by averaging a minimum of three measurements taken from SEM images of the beam fracture surface after test.

The load-displacement (F-d) curve associated with each beam bending was collected and corrected for force drift during measurement. Figure 4.4(a) shows typical F-d curves measured from the bending of pre-notched microcantilever beams. Differences in beam dimensions contribute to variations in force and indenter displacement. For example, beams composed entirely of a-C:H:Cr and Cr have longer load arms as compared to beams exposing the a-C:H:Cr/Cr/316SS interface. It is evident from Fig. 4.4(a) that the F-d curves associated with bending of pre-notched Cr beams and pre-notched a-C:H:Cr beams are linear up to the point of fracture. The F-d curves associated with the bending of a-C:H:Cr/Cr/316SS beams with pre-

notches milled into the middle of the Cr interlayers remain largely linearly up to the point of fracture, see for example three of the four F- d curves shown in Fig. 4.4(a) with Cr interlayer thicknesses of 100 nm, 200 nm, and 300 nm. Figure 4.4(a) also shows an example of exception: the F-d curve (shown in green in Fig. 4.4(a)) with a Cr interlayer thickness of 200 nm shows a clear deviation from linearity, exhibiting a linear rise in force with displacement

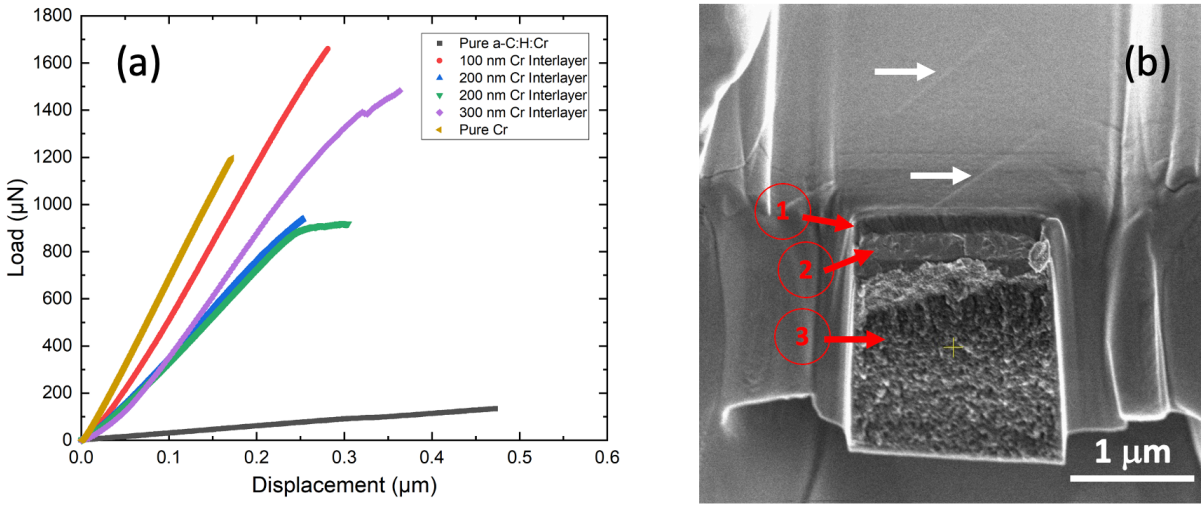

Figure 4.4. (a) Typical load-displacement curves measured from pre-notched microcantilever beam bending experiments. Different symbols shown in the legend identify measurements made on a pre-notched Cr beam, a pre-notched a-C:H:Cr beam, and a-C:H:Cr/Cr/316SS beams with pre-notches milled into the middle of the Cr interlayers; (b) SEM image of a fractured a-C:H:Cr/Cr/316SS beam with a 200 nm thick Cr interlayer. The two white arrows highlight the slip traces on the surface of the 316SS substrate formed due to loading of the cantilever in bending. The red arrows marked 1, 2, and 3 denote respectively on the fracture surface the pre-notch, fracture within the Cr interlayer, and fracture within the a-C:H:Cr layer.

followed by a force plateau. Figure 4.4(b) shows an SEM image of this particular a-C:H:Cr/Cr/316SS beam after fracture has occurred. The two white arrows highlight the slip traces on the surface of the 316SS substrate formed due to loading of the cantilever in bending, from which it is concluded that the apparent plasticity exhibited by the F-d curve is due to plasticity occurring within the 316SS region, rather than within the interface region where fracture occurred. The presently observed interfacial fractures are consistent with linear elastic

fracture mechanics, and plasticity does not dominate the interfacial fracture events. In Fig. 4.4(b), the FIB milled pre- notch region exhibits a smooth morphology that is easily distinguishable from the fracture surfaces after bending. Propagation of crack initiated from the pre-notch (delineated in Fig. 4.4(b) by arrow 1) deviated from a straight path, stayed within the Cr interlayer (delineated in Fig. 4.4(b) by arrow 2) and finished within the a-C:H:Cr layer (delineated in Fig. 4.4(b) by arrow 3).

Figure 4.5 shows typical morphologies of fractured microcantilever beams. Figure 4.5(a) shows an SEM image of a typical broken a-C:H:Cr beam. Fracture initiated from the FIB milled pre-notch and remained relatively straight while propagating through the entire beam thickness. Figures 4.5(b/c/d) show respectively SEM images of broken a-C:H:Cr/Cr/316SS beams with fractures initiated from pre-notches milled in the middle of the Cr interlayers with thicknesses of 100 nm, 200 nm, and 300 nm. The FIB milled pre-notch regions are easily distinguishable from

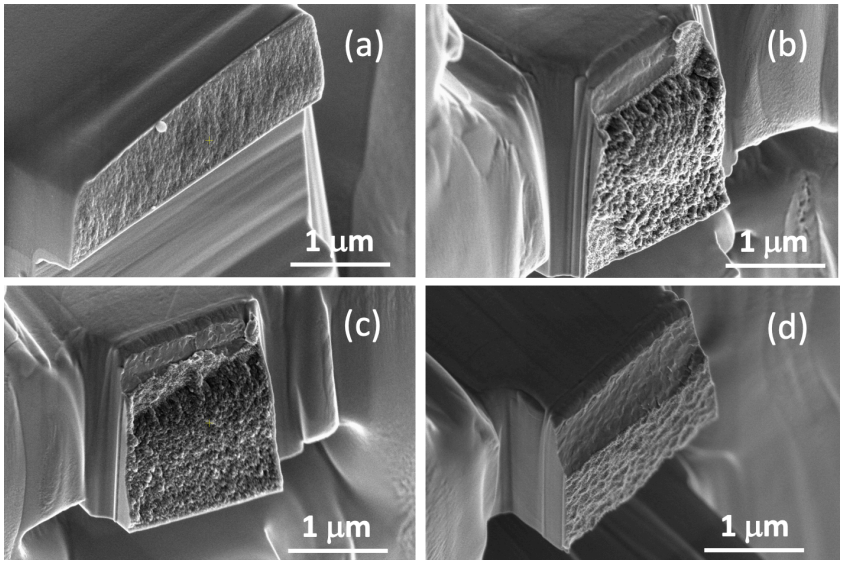

Figure 4.5. Typical morphologies of fractured micro cantilever beams with FIB milled pre-notches: (a) a pure a-C:H:Cr beam; (b/c/d) a-C:H:Cr/Cr/316SS beams with fractures initiated from pre-notches cut in the middle of the Cr interlayers of thickness (b) 100 nm; (c) 200 nm; (d) 300 nm.

the rest of the fracture surface due to morphological differences, with the FIB milled regions being smoother. While fractures initiated from the pre-notches, it is noted that they deviated from straight paths and propagated from the Cr layer into the a-C:H:Cr layers as cracks extended. This is confirmed through the SEM EDS mapping shown in Fig. 4.6. Figure 4.6(a) shows an SEM image of the fracture surface of one broken a-C:H:Cr/Cr/316SS microcantilever beam with a Cr interlayer thickness of 200 nm. Figures 4.6(b/c/d) show respectively the associated X-ray intensity maps of Cr Kα; Fe Kα; and C Kα. The Cr Kα and C Kα intensities increase toward the bottom part of the fracture surface while the Fe Kα intensity decreases, consistent with the bottom part of the fracture surface being within the a-C:H:Cr layer.

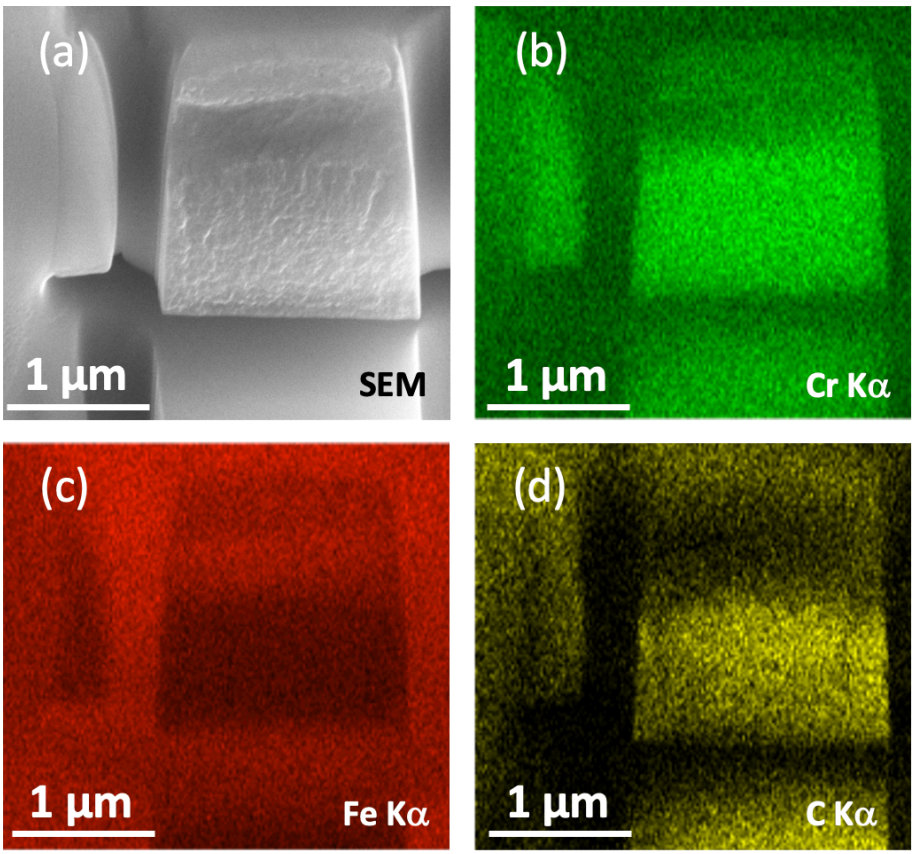

Figure 4.6. Typical EDS mapping of the interfacial fracture surface of one a-C:H:Cr/Cr/316SS microcantilever beam: (a) an SEM image of the fracture surface; (b)/(c)/(d) show respectively X-ray intensity maps of Cr Kα, Fe Kα, and C Kα.

Following Iqbal et al., the fracture toughness value is obtained from the bending fracture measurement via Equation 4.3

$$K_{IC} = \frac{FL}{BW^{\frac{3}{2}}} f(\frac{a}{W}) \text{ (Equation 4.3)}$$

where F is the fracture force and L is the load arm length or the distance between loading point and the pre-notch, and f(a/W) is a dimensionless function of a and W [36]. As both a and W are defined in the same direction, the term f(a/W) accounts for how far the pre-notch is milled through the beam. Table 4.1 shows measured K_{IC} values for the a-C:H:Cr layer, the a-C:H:Cr/Cr/316SS interfaces with varying Cr interlayer thicknesses, and the elemental Cr layer.

Table 4.1. Average fracture toughness and standard deviation of tested microcantilever beams.

	K_{IC} (MPa $m^{1/2}$)	Standard Deviation (MPa $m^{1/2}$)
a-C:H:Cr	0.80	0.15
a-C:H:Cr/Cr/316SS interface: Cr interlayer thickness 100 nm	2.02	0.36
a-C:H:Cr/Cr/316SS interface: Cr interlayer thickness 200 nm	1.52	0.17
a-C:H:Cr/Cr/316SS interface: Cr interlayer thickness 300 nm	1.91	0.24
Cr	2.50	0.38

The measured fracture toughness of Cr, 2.5 MPa $m^{1/2}$, is consistent with previously reported values for ultrafine grain Cr [45]. Figure 4.7 plots fracture toughness values for a-C:H:Cr/Cr/316SS interfacial regions as a function of the Cr interlayer thickness measured from separate beam bending experiments and illustrates the level of data scatter. Within experimental

error, there is not a noticeable trend relating interlayer thickness to measured fracture toughness of the a-C:H:Cr/Cr/316SS interfacial region.

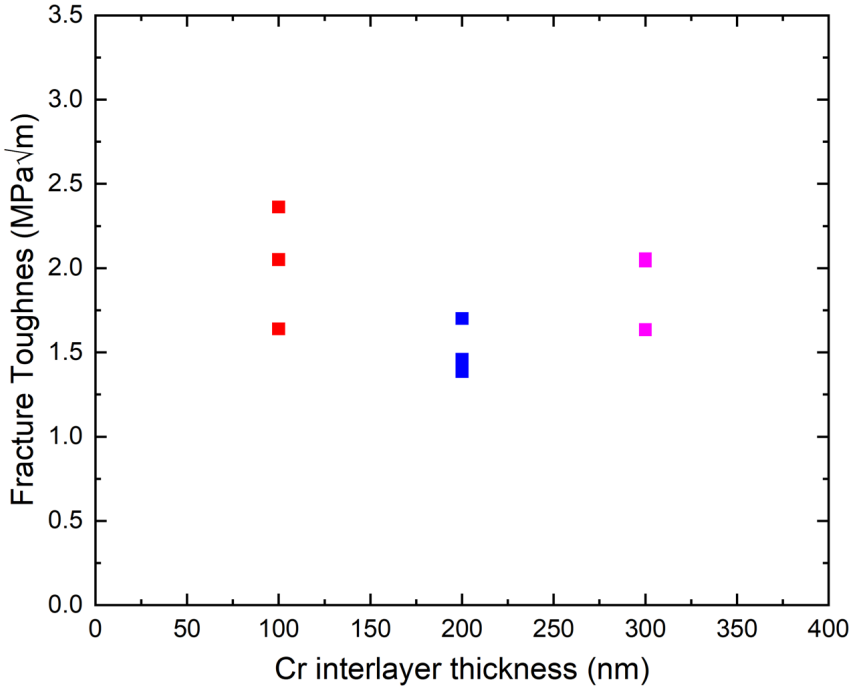

Figure 4.7. Measured fracture toughness of the a-C:H:Cr/Cr/316SS interfacial region vs. the thickness of the Cr interlayer.

4.4. Further processing of fracture toughness measurements

High resolution images of microcantilever beam fracture surfaces were taken using the Helios™ G4 PFIB/SEM. X-ray energy dispersive spectroscopy (EDS) maps of fracture surfaces were collected using an Oxford system housed on the PFIB/SEM. Area measurements on SEM images of microcantilever beam fracture surfaces were conducted using the National Institutes of Health software ImageJ.

Observations documented in Figs. 4.5 and 4.6 indicate that fracture did not occur entirely within the Cr interlayer, even though the FIB milled pre-notch was in its center. Fig. 4.8(a) shows an SEM image of a typical fracture surface, with identification of the areas corresponding to the FIB milled pre-notch, fracture within the Cr interlayer, and fracture within the a-C:H:Cr

layer. The software ImageJ was used to determine the projected area fraction of the fracture surface that occurred within the Cr interlayer and the a-C:H:Cr layer. This process was repeated for all broken a-C:H:Cr/Cr/316SS beams. Figure 4.8(b) replots data shown in Fig. 4.7 vs. the area fraction of fracture surface occurring in the Cr interlayer. The datapoints at fraction values of 0 and 1 correspond respectively to fracture toughness values measured from a-C:H:Cr beams and Cr beams. There is a clustering of data points within projected area fractions between 0.2 – 0.4 and between 0.8 – 0.9. As shown by the red line in Fig. 4.8(b), measured fracture toughness values of the a-C:H:Cr/Cr/316SS interfacial regions follow an approximately linear correlation with the area fraction, ranging between the fracture toughness of a-C:H:Cr and elemental Cr. The relatively large data scatter notwithstanding, data shown in Fig. 4.8 suggest that the measured fracture toughness of the interfacial region depends on the detailed path of the crack as it propagates through the specimen.

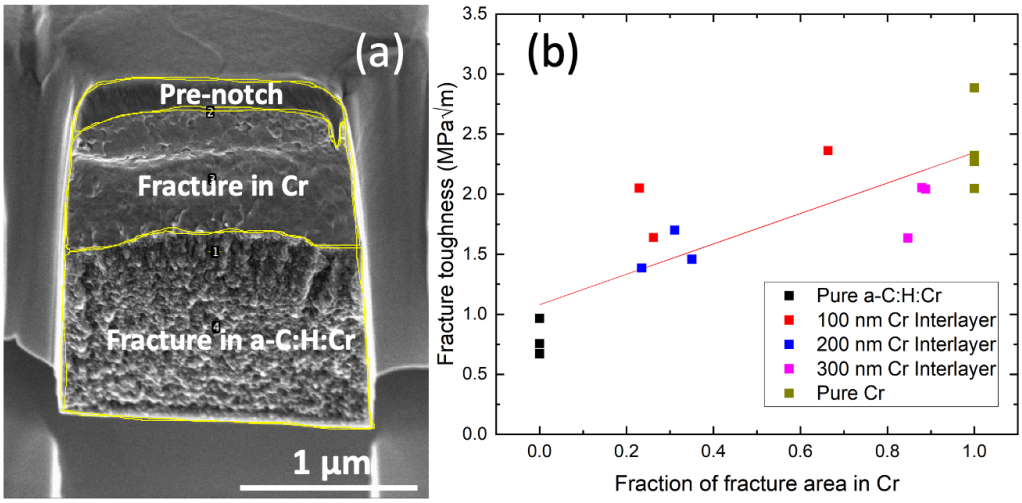

Figure 4.8. Correlation between fracture surface area and measured fracture toughness. (a) an SEM image of a typical fracture surface, with identification of the areas corresponding to the FIB milled pre-notch, fracture within the Cr interlayer, and fracture withing the a-C:H:Cr layer; (b) data shown in Figure 4.7 replotted vs. the fraction of fracture area occurring in the Cr interlayer. The data points at fractions of 0 and 1 correspond respectively to fracture toughness values measured from pure a-C:H:Cr beams and pure Cr beams.

4.5. Discussion

The hardness, indentation modulus, coefficient of friction, wear coefficient, and fracture toughness of the a-C:H:Cr/Cr/316SS film system were measured. The coating of 316SS substrates with the a-C:H:Cr/Cr coatings increased the hardness from ~4.5 GPa to ~7.5 GPa. The ratio of measured hardness to indentation modulus of 1:10 is consistent with previously measured results [43]. The presence of the a-C:H:Cr coating of the 316SS substrate resulted in a coefficient of friction near 0.2, where the value for the uncoated substrate was above 0.6. The reduction of measured coefficient of friction due to the coating of a metal containing DLC film is consistent with current literature [46]. The measured fracture toughness of the interface of the a-C:H:Cr/Cr coating and the 316SS substrate was found to have no apparent correlation to the Cr interlayer thickness.

Despite the FIB pre-notch being milled approximately in the center of the Cr interlayer for all samples, it was found that the crack tended to progress towards the a-C:H:Cr/Cr interface. It was found that the measured fracture toughness of the interface tended to vary between the measured fracture toughness of pure a-C:H:Cr and pure Cr based on the area fraction of the fracture surface that occurred in the Cr interlayer. There are several experiments that could be performed as an extension of this observation but are not within the scope of this study. One potential extension is to determine at what interlayer thickness the pre-notch no longer propagates to the DLC-interlayer interface. A more complicated extension would investigate manipulations to the deposition process to cause more of the fracture event to occur within the interlayer. With the experimental method described in this study, there is no apparent method of producing samples that will have a predetermined fracture area fraction in the Cr interlayer.

Chapter 5. Summary and Conclusions

Deposition parameters for depositing a-C:H:Cr films with a Cr interlayer on 316 stainless steel substrates were analyzed. It was found that the external deposition conditions must be manipulated to obtain a consistent internal plasma condition. The measurable variable which indicates the plasma condition is the substrate bias current. The primary method of obtaining a consistent substrate bias current is the manipulation of the applied inductively coupled plasma input power. Once this deposition parameter was consistently applied, the deposited films were consistently dense, uniform, and void free.

The deposited film system was characterized using various techniques. Scanning electron microscopy was used to visually determine that the absence of voids and the uniformity of the coating interfaces. X-ray photoelectron spectroscopy was used to determine the composition of the a-C:H:Cr film was primarily C and Cr. The presence of C-C and C-Cr bonds was observed. X-ray diffraction was used to confirm that BCC Cr was present in the coating layers. Transmission electron microscopy coupled with energy dispersive spectroscopy was used to further analyze the composition and structure of the coating system. TEM data indicates that there are nanometer scale Cr containing particulates within the film. Based on XPS and TEM diffraction data, it is unclear whether these particulates are crystalline Cr or a chromium carbide with a similar lattice parameter to Cr.

The hardness, indentation modulus, coefficient of friction, wear coefficient of the film a-C:H:Cr films were measured. The film was found to have a higher hardness than the substrate. The film was found to have a low coefficient of friction and wear rate that is consistent with other studies on the friction / wear characteristics of DLC films.

The fracture toughness of a-C:H:Cr, Cr, and the a-C:H:Cr/Cr/316SS interface were

measured via the bending of pre-notched micro-cantilever beams. No correlation between the Cr interlayer thickness and the measured interfacial fracture toughness was observed. However, it was observed that the pre-notch placed in the Cr interlayer tended to propagate towards the a-C:H:Cr / Cr interface. Utilizing EDS mapping of the fracture surface and the image processing software ImageJ, a correlation was determined. It was observed that the measured interfacial fracture toughness linearly varied from the fracture toughness of a-C:H:Cr to the fracture toughness of Cr based on the area fraction of the fracture surface occurring in Cr.

Appendix A. Publication Information

Portions of this thesis are included in a manuscript pending approval with the journal Surface & Coatings Technology. When submitting the manuscript, the author transferred copyright of the content to the publisher. The publishing agreement states that the primary author can use the content for personal use, which includes use in a thesis or dissertation. The following images display proof that the author of this thesis is the primary author of the submitted document and the portion of the personal use agreement referring to an academic thesis.

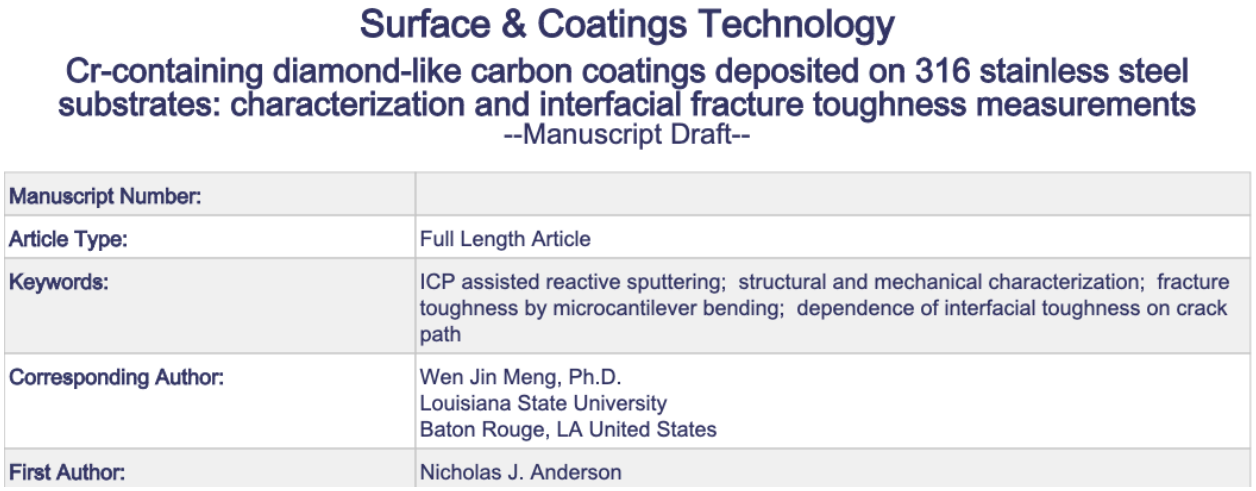

Surface & Coatings Technology

Cr-containing diamond-like carbon coatings deposited on 316 stainless steel substrates: characterization and interfacial fracture toughness measurements

--Manuscript Draft--

Manuscript Number:	
Article Type:	Full Length Article
Keywords:	ICP assisted reactive sputtering; structural and mechanical characterization; fracture toughness by microcantilever bending; dependence of interfacial toughness on crack path
Corresponding Author:	Wen Jin Meng, Ph.D. Louisiana State University Baton Rouge, LA United States
First Author:	Nicholas J. Anderson

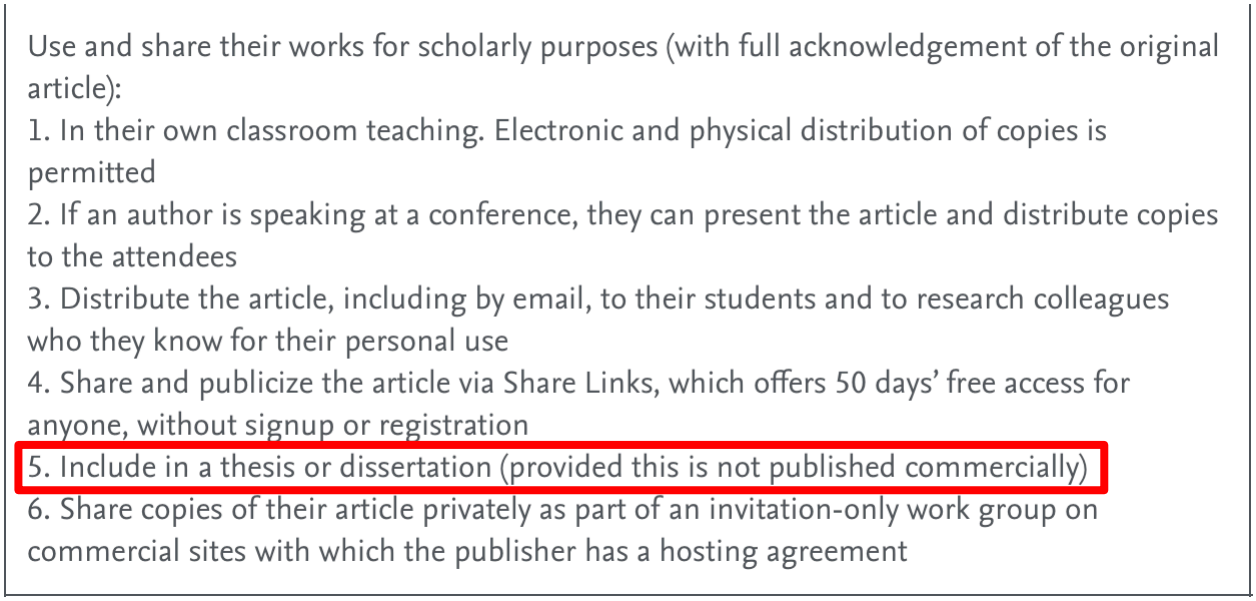

Use and share their works for scholarly purposes (with full acknowledgement of the original article):

1. In their own classroom teaching. Electronic and physical distribution of copies is permitted
2. If an author is speaking at a conference, they can present the article and distribute copies to the attendees
3. Distribute the article, including by email, to their students and to research colleagues who they know for their personal use
4. Share and publicize the article via Share Links, which offers 50 days' free access for anyone, without signup or registration
5. Include in a thesis or dissertation (provided this is not published commercially)
6. Share copies of their article privately as part of an invitation-only work group on commercial sites with which the publisher has a hosting agreement

References

1. Ohtake et al., Properties and Classification of Diamond-Like Carbon Films, Materials, vol. 14, no 2, Jan. 2021.

2. Wang, Shan, Guo, DLC-Coated Tools for Microforming, Micromanufacturing Engineering and Technology, 2nd Edition, 2015

3. Donnet, Erdemir, Tribology of Diamond-Like Carbon Films: Fundamentals and Applications, 1st Edition, Springer Science, 2008

4. Bewilogua, Hofmann, History of diamond-like carbon films – From first experiments to worldwide applications, Surface and Coatings Technology, Vol. 242, 2014

5. Corbella et al., Preparation of metal (W, Mo, Nb, Ti) containing a-C:H films by reactive magnetron sputtering, Surface and Coatings Technology, Vol. 177-178, 2004.

6. Wang et al., Structure and mechanical properties of W incorporated diamond-like carbon films prepared by a hybrid ion beam deposition technique, Carbon, Vol 44, 2006.

7. Guo, Ke, Wang, Incorporated W Roles on Microstructure and Properties of W-C:H films by a Hybrid Linear Ion Bean Systems, Journal of Nanomaterials, 2013.

8. Paul et al, Modulation of residual stress in diamond like carbon films with incorporation of nanocrystalline gold, Applied Surface Science, Vol. 257, 2011.

9. Paul, Diamond-Like-Carbon Coatings for Advanced Biomedical Applications, Glob J Nano., 2017.

10. Okpalugo, Ogwu, DLC thin films for implantable medical devices, Thin Film Coatings for Biomaterials and Biomedical Applications, 2016.

11. Nagashima et al., Diamond-Like Carbon Coatings for Joint Arthroplasty, Material for Total Joint Arthroplasty, Chapter 13, 2015.

12. Rothammer et al., Amorphous Carbon Coatings for Total Knee Replacements – Part II: Tribological Behavior, Polymers, 2021.

13. Love et al., Diamond like carbon coatings for potential application in biological implants – a review, Tribology International, 63, 2012.

14. Folea et al., An Overview of DLC Coatings on Cutting Tools Performance, Academic Journal of Manufacturing Engineering, 8, 2010.

15. Wang et al., Modification of Diamond like Carbon Coating and the Performance in Machining Applications: A Review, Coatings, 2022.

16. Wu, Cheng, An investigation on the micro cutting performance of diamond-like carbon coatings

using finite element method, The International Journal of Advanced Manufacturing Technology, 73, 2014

17. Luo et al., Diamond and diamond-like carbon MEMS, Journal of Micromechanics and Microengineering, 17, 2007.

18. Santra et al., Chapter 18 Diamond, Diamond-Like Carbon (DLC) and Diamond-Like Nanocomposite (DLN) Thin Films for MEMS Applications, Microelectromechanical Systems and Devices, 2011

19. Lu et al., Micromechanical properties of hydrogenated diamond-like carbon multilayers, Surface and Coatings Technology, Vol. 201, 2006.

20. Aisenberg, Chabot, Ion-Beam Deposition of Thin Films of Diamondlike Carbon, Journal of Applied Physics, Vol. 42, 1971.

21. Moriguchi et al., History and Applications of Diamond-Like Carbon Manufacturing Processes, SEI Technical Review, Num. 82, 2016.

22. Rabadzhiyska et al., Characterization of Diamond-like carbon films produced by electron-beam physical vapor deposition, Materialstoday: Proceedings, Vol. 67, 2022.

23. Huang et al., Wear-resistant multilayered diamond-like carbon coating prepared by pulse biased arc ion plating, Diamond and Related Materials, 10, 2001.

24. Zhen-Yu et al., Tribological properties of diamond-like carbon films deposited by pulsed laser arc deposition, Chinese Physics, Vol. 16, 12, 2007.

25. Ohring, Material science of thin films: Deposition and structure, 2nd Edition, San Diego: Academic Press., 2001.

26. Hain et al., From pulsed-DCMS and HiPIMS to microwave plasma-assisted sputtering: Their influence on the properties of diamond-like carbon films, Surface and Coatings Technology, Vol. 432, 2022.

27. ASTM Standard Procedure D4541 – 17, Standard test method for pull-off strength of coatings using portable adhesion testers, ASTM International, 2017.

28. J.M. Arenas, J.J. Narbon, C. Alia, Optimum adhesive thickness in structural adhesives joints using statistical techniques based on Weibull distribution, Int. J. Adhes. Adhes. 30, 160-165 (2010).

29. ASTM C1624-22, Standard Test Method for Adhesion Strength and Mechanical Failure Modes of Ceramic Coatings by Quantitative Single Point Scratch Testing

30. Ast et al., A review of experimental approaches to fracture toughness evaluation at the micro-scale, Materials and Design, Vol. 173, 2019.

31. Iqbal et al., In situ micro-cantilever tests to study fracture properties of NiAl single crystals, Acta Materialia, Vol. 60, 2012.

32. Riedl et al., A novel approach for determining fracture toughness of hard coatings on the micrometer scale, Scripta Materialia, Vol. 67, 2012.

33. Awaji, Sakaida, V-Notch Technique for Single-Edge Notched Beam and Chevron Notch Methods, Journal of the American Ceramic Society, Vol. 73, 2005.

34. Okamoto et al., Fracture Toughness of the Fe-Zn Intermetallic Compounds Measured by Bend Testing of Chevron-Notched Single-Crystal Microbeams, ISIJ International, Vol. 58, 2018.

35. Delfani-Abbariki et al., Enhancing the adhesion of diamond-like carbon films to steel substrates using silicon-containing interlayers, Surface and Coatings Technology, Vol. 350, 2018.

36. Maiti, Mills, Wear Properties of Diamond-like-carbon coatings with Silicon and Chromium as adhesion layer using a High Frequency Reciprocating Rig, Journal of Engineering Tribology, Vol. 231, 2017.

37. Kaneko et al., Preparation of Diamond-Like Carbon on Ti Film with Tetramethylsilane Buffer Layer, Japanese Journal of Applied Physics, Vol. 52, 2013.

38. A.G. Evans, J.W. Hutchinson, Y. Wei, Interface adhesion: effects of plasticity and segregation, Acta mater. 47, 4093-4113 (1999).

39. W.J. Meng, T.J. Curtis, L.E. Rehn, P.M. Baldo, Temperature dependence of inductively coupled plasma assisted growth of TiN thin films, Surf. Coat. Technol. 120/121, 206–212 (1999).

40. Moulder et al., Handbook of X-ray Photoelectron Spectroscopy, Perkin-Elmer Corporation, 1992.

41. Callister, Rethwisch, Materials Science and Engineering: An Introduction, 9th Edition, John Wiley & Sons, p. 89, 2014.

42. Oliver, Pharr, Measurement of hardness and elastic modulus by instrumented indentation: Advances in understanding and refinements to methodology, Journal of Materials Research, 2003.

43. W.J. Meng, T.J. Curtis, L.E. Rehn, P.M. Baldo, Plasma-assisted deposition and characterization of Ti-containing diamondlike carbon coatings, J. Appl. Phys. 83, 6076- 6081 (1998).

44. D.M. Cao, B. Feng, W.J. Meng, L.E. Rehn, P.M. Baldo, M.M. Khonsari, Friction and wear characteristics of ceramic nanocomposite coatings: titanium carbide/amorphous hydrocarbon, Appl. Phys. Lett. 79, 329-331 (2001).

45. I. Issa, A. Hohenwarter, R. Fritz, D. Kiener, Fracture properties of ultrafine grain chromium correlated to single dislocation processes at room temperature, J. Mater. Res. 34, 2370- 2383 (2019).

46. Huang et al., Synthesis of copper nanoparticles containing diamond-like carbon films by electrochemical method, Electrochemistry Communications, Vol. 8, 2006.

Vita

Nicholas Anderson earned his Bachelor's of Science in Mechanical Engineering from Louisiana State University in May 2022. Nicholas is a participant in the Accelerated Master's of Science in Mechanical Engineering program offered by Louisiana State University's Department of Mechanical and Industrial Engineering. He has worked as a member of Dr. Meng's research group since the summer of 2021. The focus of his research has been the vapor deposition and material characterization of thin films. Nicholas anticipates graduating in May 2023.